Corrosion-Assisted Heterogeneous Nucleation for CoNiFe Layered Double Hydroxides toward High-Current Methanol Oxidation

*Ye Li,[a] Yonglin Wang,[a] Xingyu Luo,[b] Hanlu Xie,[a] Yuchen Wei,[a] Yuan Gao,[a] Peng Xiao,[*b] and Yunhuai Zhang[*a]*

[a] College of Chemistry and Chemical Engineering, Chongqing University, Chongqing, 401331, China.

[b] College of Physics, Chongqing University, Chongqing 401331, China.

[*]Corresponding authors E-mail: zyh2031@cqu.edu.cn (Y. Zhang), xiaopeng@cqu.edu.cn (P. Xiao)

I. Experimental Section

1. Materials and Characterizations

***Materials*:**Cobaltous(II) nitrate hexahydrate ($Co(NO_3)_2·6H_2O$, Macklin, 99%, CAS no. 10026-22-9), iron(II) sulfate ($FeSO_4·7H_2O$, Aladdin Industrial, ≥99.0%, CAS no. 7782-63-0), ethyl alcohol (CH_3CH_2OH, KESHI, 99.7%, CAS no. 64-17-5), potassium hydroxide (KOH, Macklin, 95%, CAS no. 1310-58-3), methanol (CH_3OH, MeOH, Macklin, 99.5%, CAS no. 67-56-1), acetone (CH_3COCH_3, CHUANDONG CHEMICAL, 99.5%, CAS no. 67-64-1) and hydrochloric acid (HCl, CHUANDONG CHEMICAL, 36%, CAS no. 7647-01-0) were used without any pre-treatment or purification, deuterium oxide (D_2O, Meryer (Shanghai) Chemical Technology Co., Ltd, 99.9%, CAS no. 7789-20-0), dimethyl sulfoxide (DMSO, Macklin, ≥99.9%, CAS no. 67-68-5).

2. Material preparation

Pretreatment of the nickel foam (NF): The NF (thickness of 1 mm) was first sonicated in acetone for 15 min, then in 3 mol L^{-1} HCl for another 15 min to remove organic residues and surface oxides. Subsequently, it was thoroughly rinsed with distilled water and finally dried in a vacuum oven at 60 ℃ for 12 h.

Synthesis of NiFe LDH/NF: A 0.085 M $FeSO_4·7H_2O$ aqueous solution was introduced dropwise into anhydrous ethanol at a 1:3 volume ratio under vigorous stirring. A pretreated NF substrate was then fully immersed in the resulting mixture and maintained at 35 °C for 24 h. Afterward, the sample was thoroughly rinsed with deionized water and dried in a vacuum oven at 60 °C for 12 h to yield NiFe LDH/NF(denoted as NiFe), with a catalyst loading of ~3 mg cm^{-2}

Synthesis of CoNiFe LDH/NF: For the preparation of CoNiFe LDH, an aqueous solution of 0.085 M $FeSO_4·7H_2O$ was slowly dripped into a vigorously stirred solution of $Co(NO_3)_2·6H_2O$ in ethanol at a volume ratio of 1:3. For comparative analysis, the concentration of $Co(NO_3)_2·6H_2O$ in ethanol was 0.1 M, 0.2 M and 0.3 M respectively. A piece of pre-treated NF was then completely immersed in the precursor and maintained at 35 °C for 24 h. After washing by deionized water and drying in a vacuum oven at 60 °C for 12 h, CoNiFe LDH was obtained and denoted as CoNiFe-1, CoNiFe-2 and CoNiFe-3 respectively according to the concentration of $Co(NO_3)_2·6H_2O$ in ethanol. The mass loading of the catalyst on NF was about 4~6 mg·cm^{-2}. To prepare CoNiFe LDH on a 12 × 12 cm piece of NF, the same reagent concentrations and volume ratio as those used for CoNiFe-2 were employed.

3. Characterization

The morphology of the catalysts was investigated using a Japan Electron Optics Laboratory (JEOL) JSM-7800F field-emission scanning electron microscope (FE-SEM). Microstructural analysis was performed by transmission electron microscopy (TEM) on a Thermo Fisher Scientific Talos F200S instrument. Site-specific sample preparation was carried out using a Thermo Fisher Scientific Helios 5 CX focused ion beam (FIB) system. Crystalline structure was characterized by X-ray diffraction (XRD) on a PANalytical X'Pert Powder diffractometer using Cu Kα radiation (λ = 1.5406 Å) with a scanning rate of 2° min^{-1}. Elemental quantification of Co, Ni and Fe was determined by inductively coupled plasma optical emission spectrometry (ICP-OES) using a Thermo Fisher Scientific ICAP 6300 DUO instrument. Fe K-edge measurement was performed with Si(111) crystal monochromators at the BL14W beamlines at the Shanghai Synchrotron Radiation Facility (SSRF). Before the measurement, powder samples were pressed into thin sheets with 1 cm in diameter and contained in PTFE and sealed using 3M Scotch tape film. Fe-edge extended X-ray absorption fine structure (EXAFS) spectra were recorded in transmission mode. The Fourier transform infrared (FTIR) spectra were obtained on a Thermo Fisher Scientific Nicolet iS50 spectrometer equipped with an ATR accessory, scanning from 4000 to 400 cm^{-1} with a resolution of 4 cm^{-1}. Raman spectra were acquired on a HORIBA Jobin Yvon LabRAM HR Evolution spectrometer equipped with a 532 nm laser. Surface chemical composition was analyzed by X-ray photoelectron spectroscopy (XPS) on a Thermo Scientific Nexsa system. Surface wettability was evaluated through contact angle measurements performed on a DataPhysics OCA 20 system, where both the water droplet contact angle on the catalyst surface and the underwater bubble contact angle were measured. *In situ* attenuated total reflection surface-enhanced infrared absorption spectroscopy (ATR-SEIRAS) was performed using a Bruker INVENIO S FTIR equipped with a liquid-nitrogen-cooled mercury cadmium telluride detector. The working electrode was prepared by drop-casting a slurry of the catalyst powder onto a silicon ATR prism onto which a gold nanofilm had been chemically deposited. A platinum foil and an Hg/HgO electrode (in 1 M KOH) served as the counter electrode and reference electrode, respectively, in a single-compartment electrochemical cell. The spectral resolution was set to 16 cm^{-1}, and each spectrum was acquired over approximately 25 s simultaneously with linear sweep voltammetry.

4. Electrochemical measurements

All electrochemical measurements were conducted using CHI 660D and CHI 1130D electrochemical workstations (CH Instruments, Inc.) in a standard three-electrode

configuration. The working electrode was CoNiFe LDH/NF with a geometric area of 1 cm^2, a platinum mesh served as the counter electrode, and a Hg/HgO electrode (in 1 M KOH) was used as the reference electrode. The electrolytes consisted of either 1 M KOH aqueous solution or 1 M KOH with 1 M CH_3OH. All reported potentials were converted to the reversible hydrogen electrode (RHE) scale according to the equation:[1]

$$E_{RHE} = E_{Hg/HgO} + 0.098 + 0.059 \times pH \quad (1)$$

The distance between the working electrode and the reference electrode was maintained at approximately 2 mm. Linear sweep voltammetry (LSV) was performed at a scan rate of 5 mV s^{-1} with no iR compensation. Potentiostatic electrochemical impedance spectroscopy (PEIS) was measured at the potential corresponding to a current density of 10 mA cm^{-2} (*vs*. Hg/HgO), over a frequency range from 100 kHz to 0.01 Hz. The electrochemical active surface area (ECSA) was estimated via cyclic voltammetry (CV) by scanning within a non-Faradaic potential region (±0.05 V around the open circuit potential *vs*. Hg/HgO) at scan rates of 20, 40, 60, 80, and 100 mV s^{-1} to determine the double-layer capacitance (C_{dl}). Subsequently, ECSA is determined as ECSA = AC_{dl}/C_s, where A is thegeometric area of the catalyst and C_S is the specific capacitance (C_S = 0.04 mF cm^{-2}).

Methanol oxidation reaction (MOR) stability was evaluated by chronoamperometry at a fixed potential of 0.45 V *vs*. Hg/HgO.

5. Product quantification

The liquid products from methanol oxidation were analyzed by ^1H and ^{13}C nuclear magnetic resonance (NMR) spectroscopy on a Bruker AVANCE NEO 400 MHz spectrometer. For NMR sample preparation, 0.5 mL of electrolyte was mixed with 150 μL of D_2O and 0.1 mL of an aqueous internal standard solution containing 0.5 μL mL^{-1} DMSO. The concentration of electrooxidation products was quantified by comparing the integrated NMR peak areas of the products with that of the internal standard.[2, 3]

$$FE(HCOO^-,\%) = \frac{C_{formate} \times V_{electrolyte} \times 4 \times F}{Q} \times 100\% \quad (2)$$

Where $C_{formate}$ is the concentration of $HCOO^-$ (mmol L^{-1}) measured from the solution in the battery anode chamber, which is the ^{1}HNMR data. $V_{electrolyte}$ is the volume of the electrolyte (0.07 L), 4 denotes the number of electrons transferred, F represents the Faraday constant (96,485 C mol^{-1}), and Q is the passed charge (C).

$$FE(H_2\&O_2,\%) = \frac{\frac{PV}{RT} \times z \times F}{Q} \times 100\% \quad (3)$$

The Faradaic efficiencies (FE) for hydrogen and oxygen generation were calculated based on the volume of generated gas. In the calculation, P is the atmospheric pressure during the reaction (kPa), V is the volume of the collected gas (L), R is the ideal gas constant (8.314 kPa L mol^{-1} K^{-1}), T is the reaction temperature (K), z is the number of electrons transferred per molecule (for example, $z = 2$ for H_2 evolution and $z = 4$ for O_2 evolution), F is the Faraday constant (96,485 C mol^{-1}), and Q is the total charge passed during electrolysis.

II. Supplementary Figures and Tables

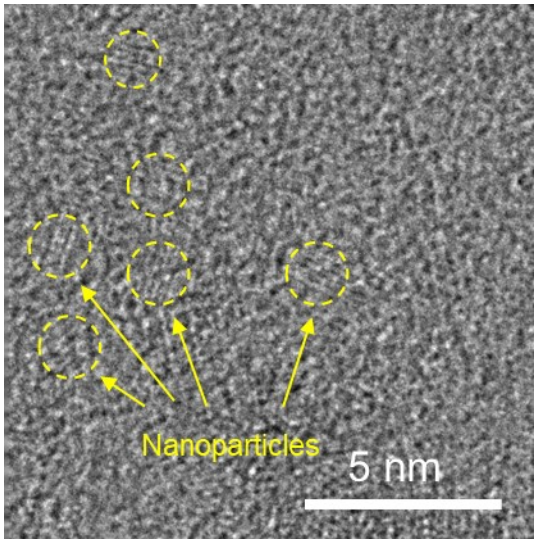

Figure S1. HRTEM image of insoluble nanoparticles.

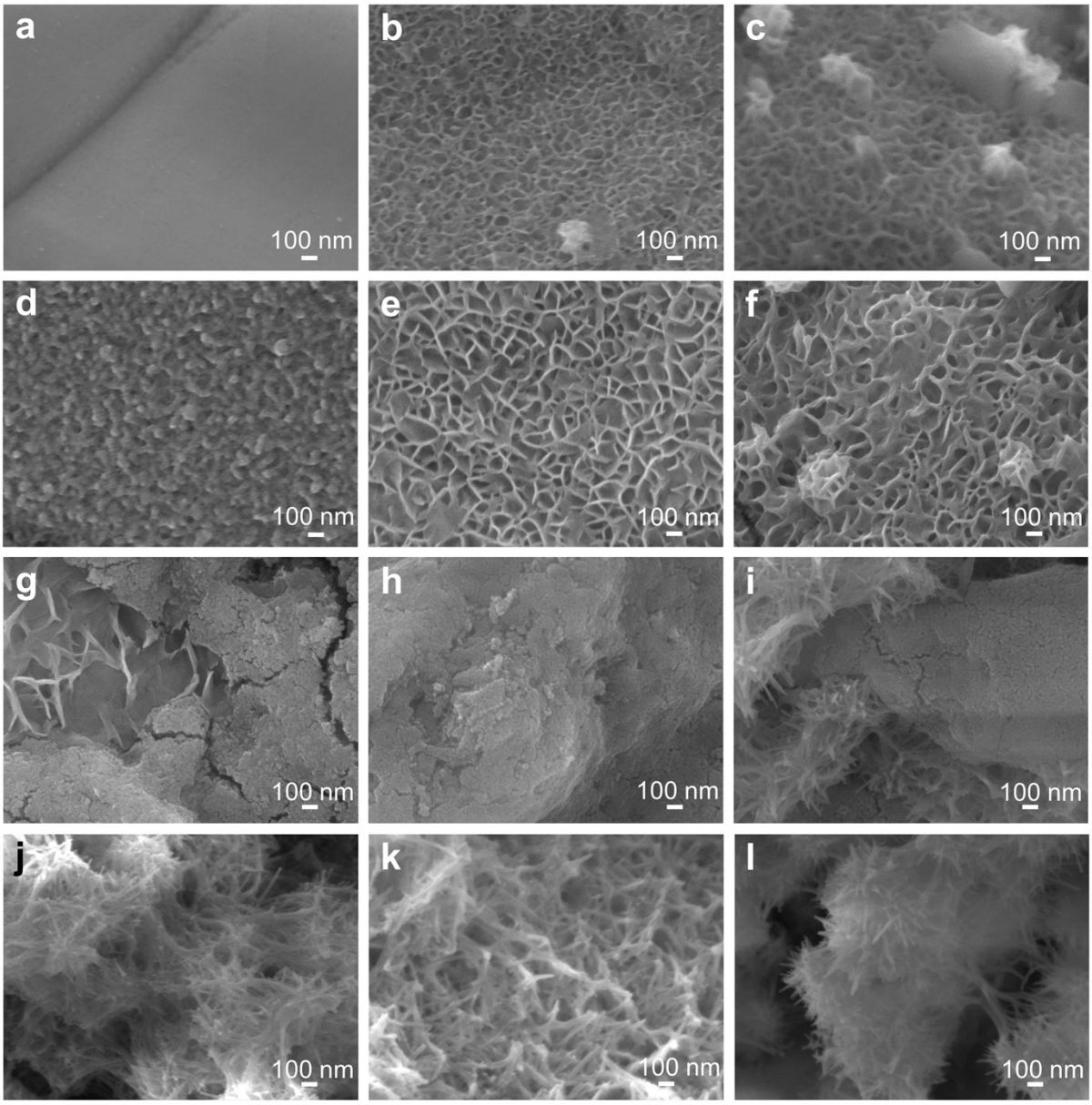

Figure S2. SEM images of CoNiFe LDH/NF under different etching durations, (a) 0 min; (b) 1 min; (c) 5 min; (d) 10 min; (e) 30 min; (f) 1 h; (g) 2 h; (h) 4 h; (i) 8 h; (j) 16 h; (k) 24 h; (l) 36 h.

Initially, the NF substrate exhibits a smooth and flat surface (Figure S2a). After 1 min of etching, distinct corrosion pits can be observed, likely due to the oxidation of Fe^{2+} to Fe^{3+} in the solution under vigorous stirring, which triggers a replacement reaction with the NF, marking the onset of the etching process. After 30 min etching, as shown in Figure S2e, a nanosheet structure begins to grow in situ on the substrate surface, indicating the formation and assembly of the LDH phase. After etching 2 hours, a large number of nanoparticles agglomerate on the surface of the nanosheets (Figure S2g). As the etching time extends to 8 hours, elongated

needle-like structures are observed (Figure S2i). With prolonged etching time, both the density and size of these needle-like structures increase significantly, ultimately forming a composite morphology dominated by a needle-like nanoarray.

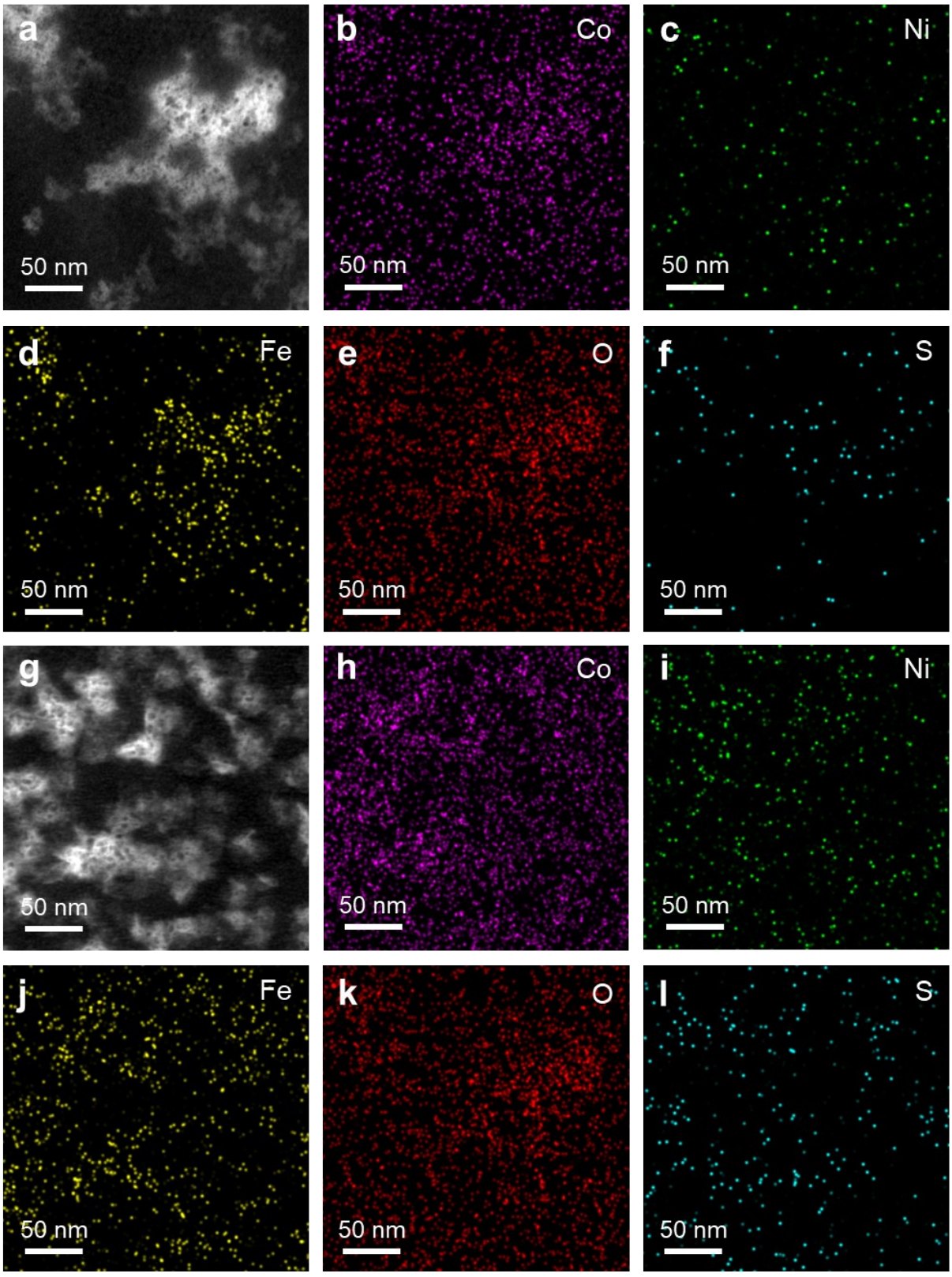

Figure S3. (a) HAADF-TEM image of nanoparticles in the heterogeneous solution after etching for 10 min; and (b-f) corresponding EDS mapping images. (g) HAADF-TEM image of nanoparticles in the heterogeneous solution after etching for 4 h; and (h-l) corresponding EDS mapping images.

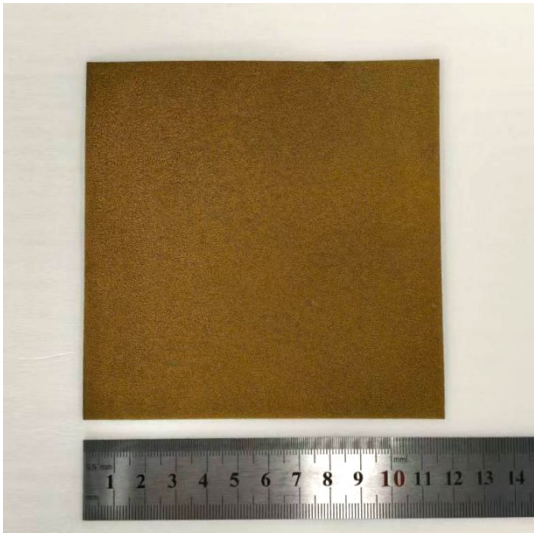

Figure S4. Photo of CoNiFe-2 with a size of 12 cm × 12 cm.

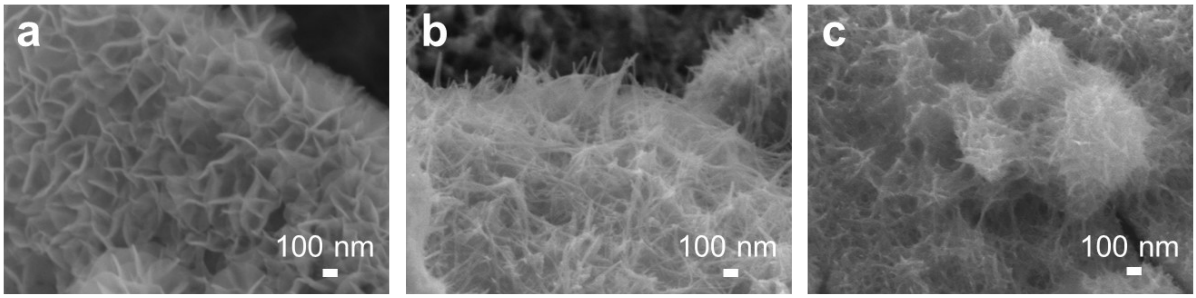

Figure S5. SEM image of (a) NiFe; (b) CoNiFe-1 and (c)CoNiFe-3.

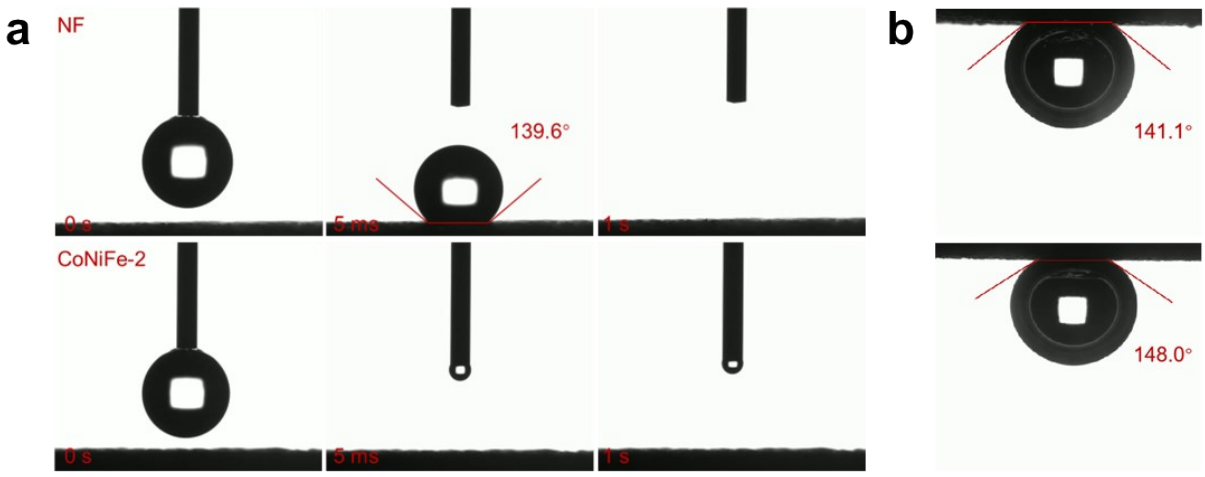

Figure S6. The wetting properties of the NF and the CoNiFe-2 electrode. (a) comparison of the hydrophilicity of different materials; (b) comparison of the aerophobicity underwater of different materials.

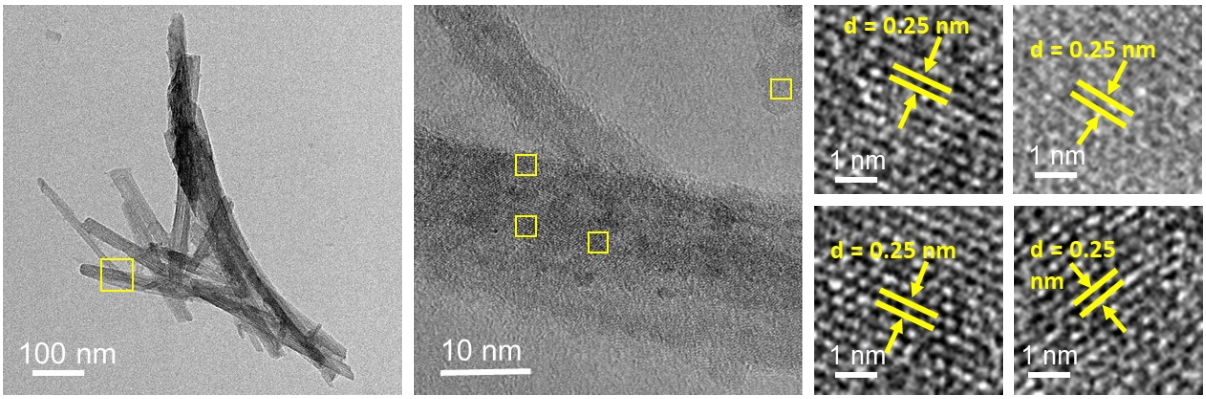

Figure S7. TEM image of CoNiFe-2.

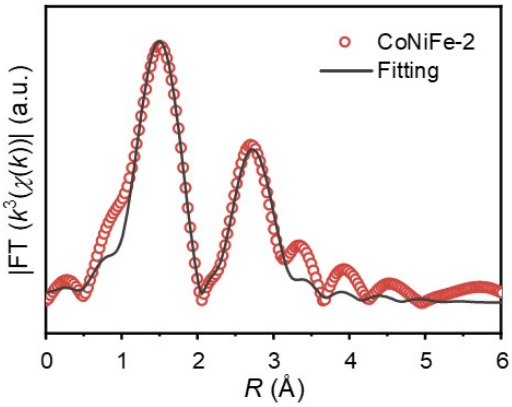

Figure S8. FT-EXAFS fitting spectrum of the Fe K-edge for CoNiFe-2.

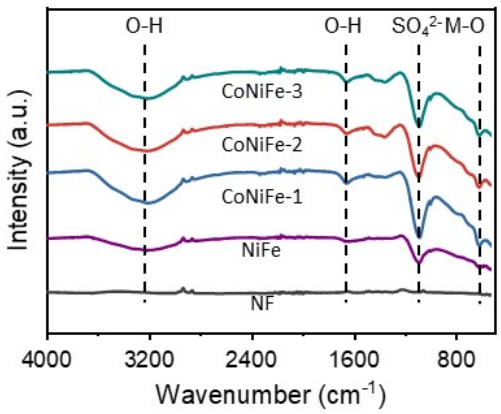

Figure S9. FTIR spectra of CoNiFe-3, CoNiFe-2, CoNiFe-1, NiFe and NF.

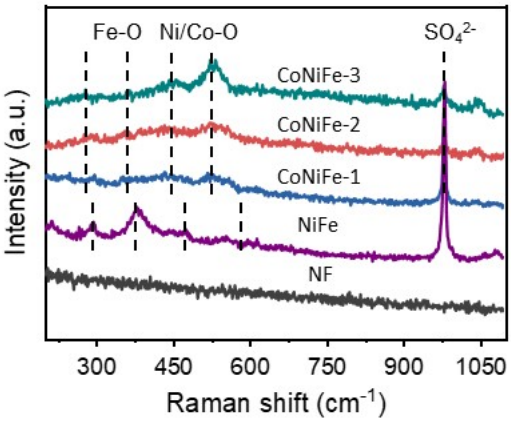

Figure S10. Raman spectra of CoNiFe-3, CoNiFe-2, CoNiFe-1, NiFe and NF.

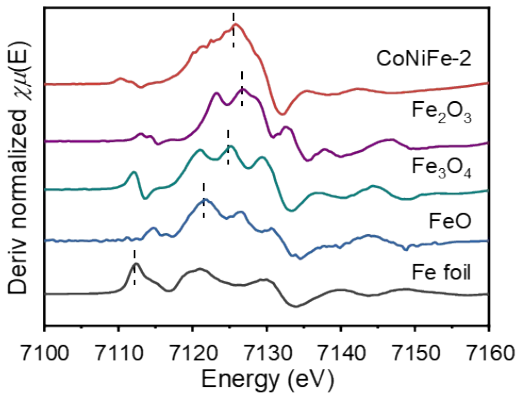

Figure S11. First-derivative XANES spectra of Fe foil, FeO, Fe_2O_3, Fe_3O_4 and CoNiFe-2.

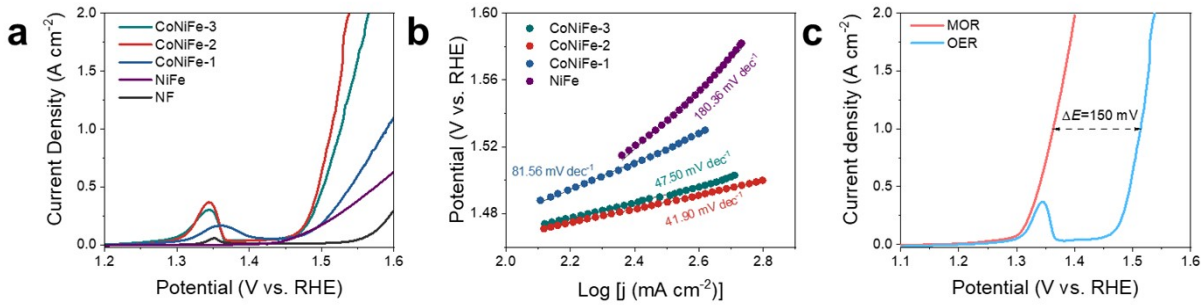

Figure S12. (a) LSV polarization curves of NiFe and CoNiFe catalysts in a 1 M KOH solution, and (b) the corresponding Tafel plots for each catalyst. (c) LSV curves of CoNiFe-2 in 1 M KOH with and without addition of 1 M MeOH.

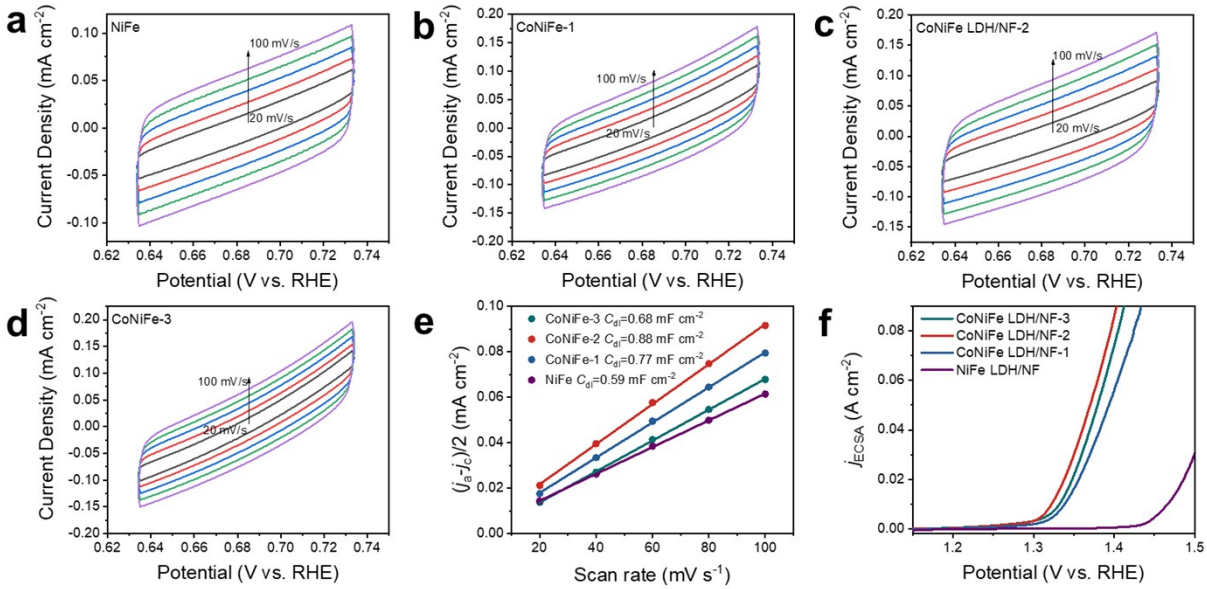

Figure S13. CV curves recorded at different scan rates from 20 to 100 mV s^{-1} within the non-Faradaic potential range for (a) NiFe, (b) CoNiFe-1, (c) CoNiFe-2 and (d) CoNiFe-3. (e) C_{dl} value of different materials. (f) LSV curves normalized by the ECSA.

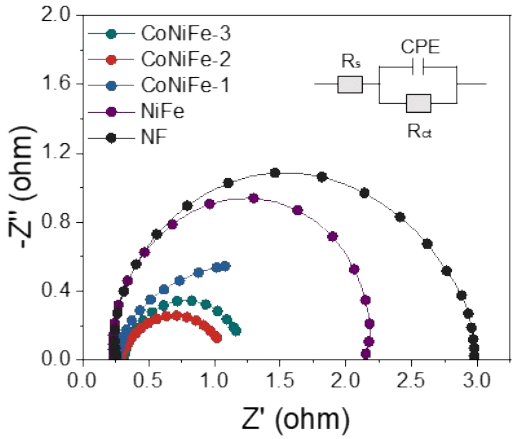

Figure S14. EIS data of NiFe and CoNiFe catalysts, and the inset shows the fitting circuit.

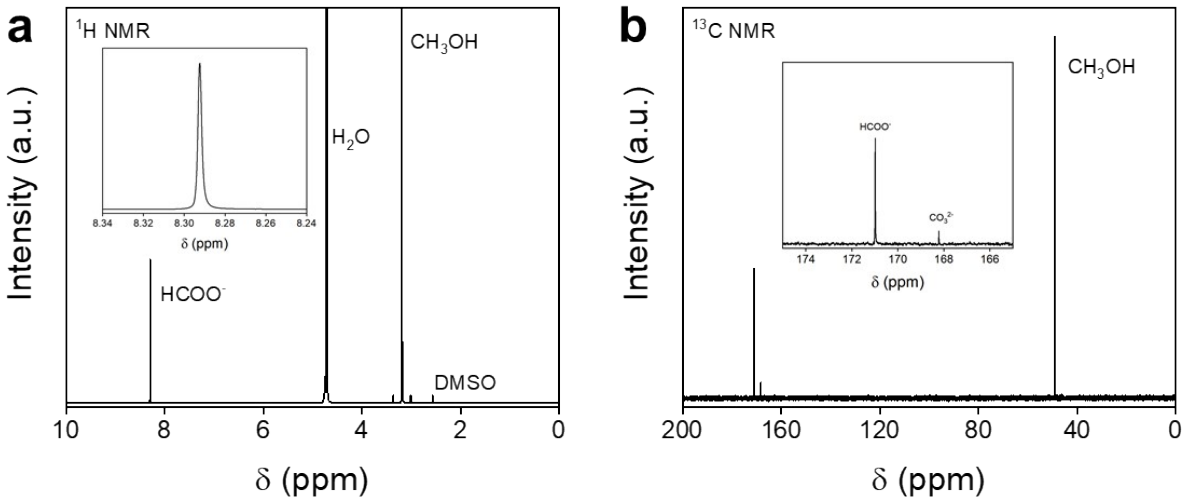

Figure S15. (a) ^{1}H NMR, (b) ^{13}C NMR measurements of methanol oxidation to formate on anode at 1.37 V *vs*. RHE in 1 M KOH + 1M MeOH solution.

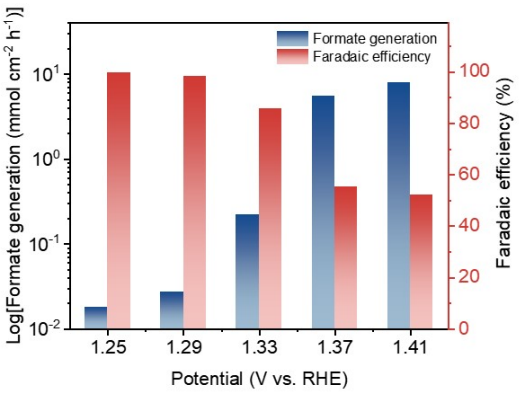

Figure S16. The rate of formate production by using CoNiFe-2 catalyst under different voltages in 1M KOH + 1M MeOH solution.

Figure S17. Photo of the H-type electrolytic cell used in the full water electrolysis/MOR-assisted hydrogen evolution device.

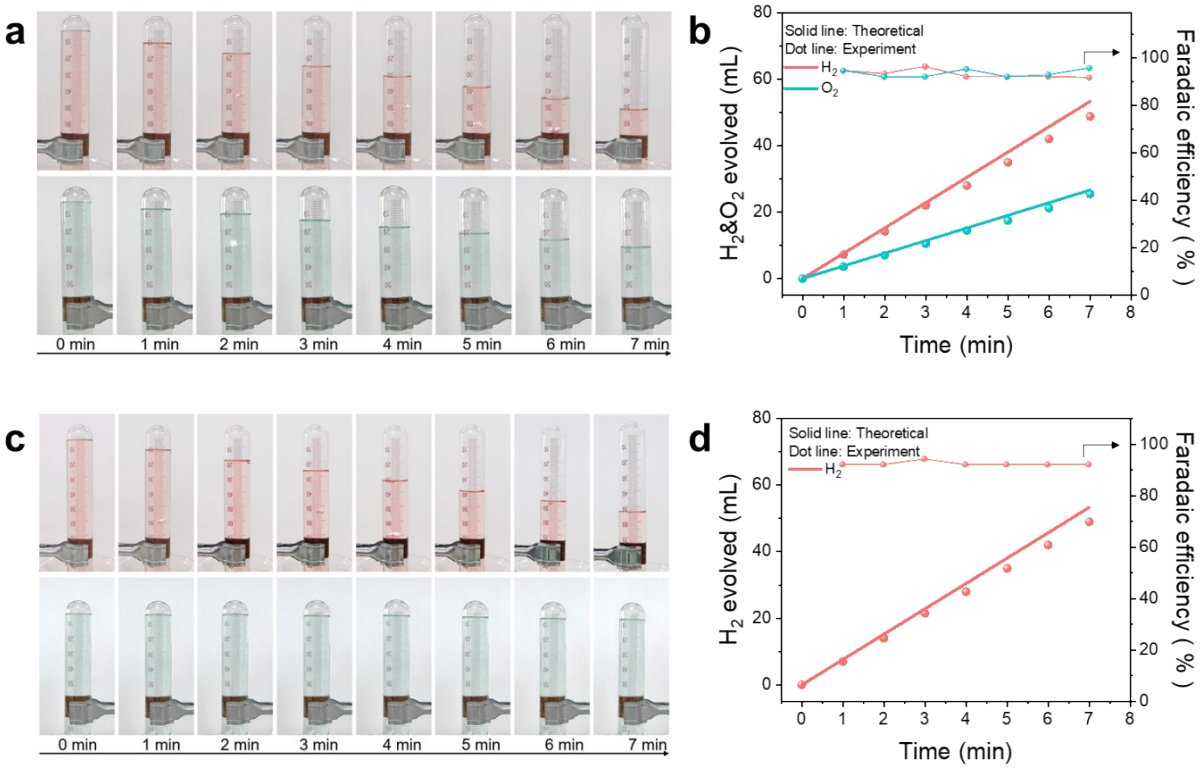

Figure S18. (a) Photos of the collected gas and (b) evolved gas volume and Faradaic efficiency for overall water splitting using CoNiFe-2 as the anode. (c) Photos of the collected gas and (d) evolved gas volume and Faradaic efficiency for MOR-assisted H_2 production. The cathodic (red) and anodic (green) products are shown.

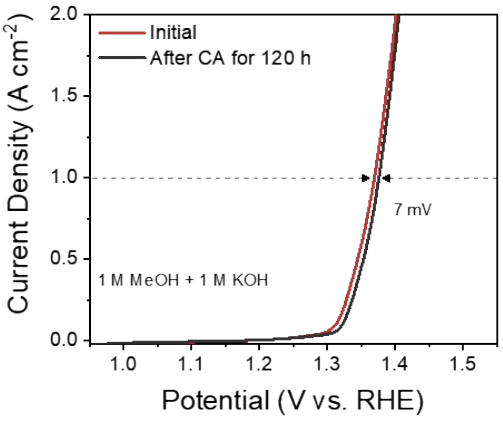

Figure S19. LSV curves before and after stability test.

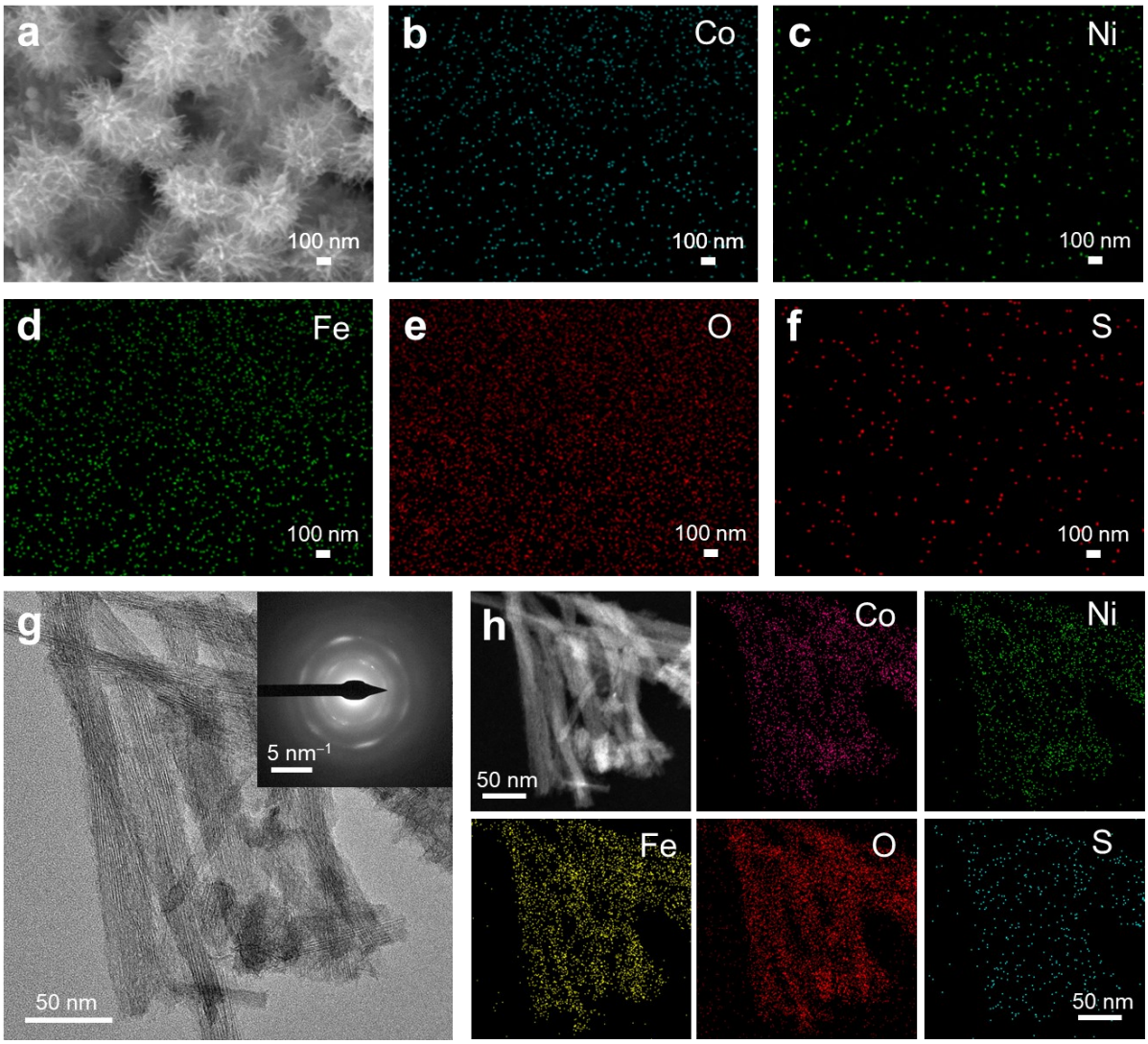

Figure S20. (a) SEM image and (b-f) corresponding EDS mapping images of CoNiFe-2 after MOR stability test. (g) TEM image (inset: corresponding SAED pattern), (h) HAADF-STEM image and the corresponding EDS elemental mapping images of CoNiFe-2 catalyst after MOR stability test.

Figure S20 shows that the catalyst largely preserves its original needle-like morphology after prolonged operation, with no obvious signs of morphological transformation or structural collapse. In addition, the corresponding EDS elemental maps reveal that Co, Ni, Fe, O, and S remain homogeneously distributed across the needle-like regions, indicating that the elemental distribution is largely maintained after long-term electrolysis.

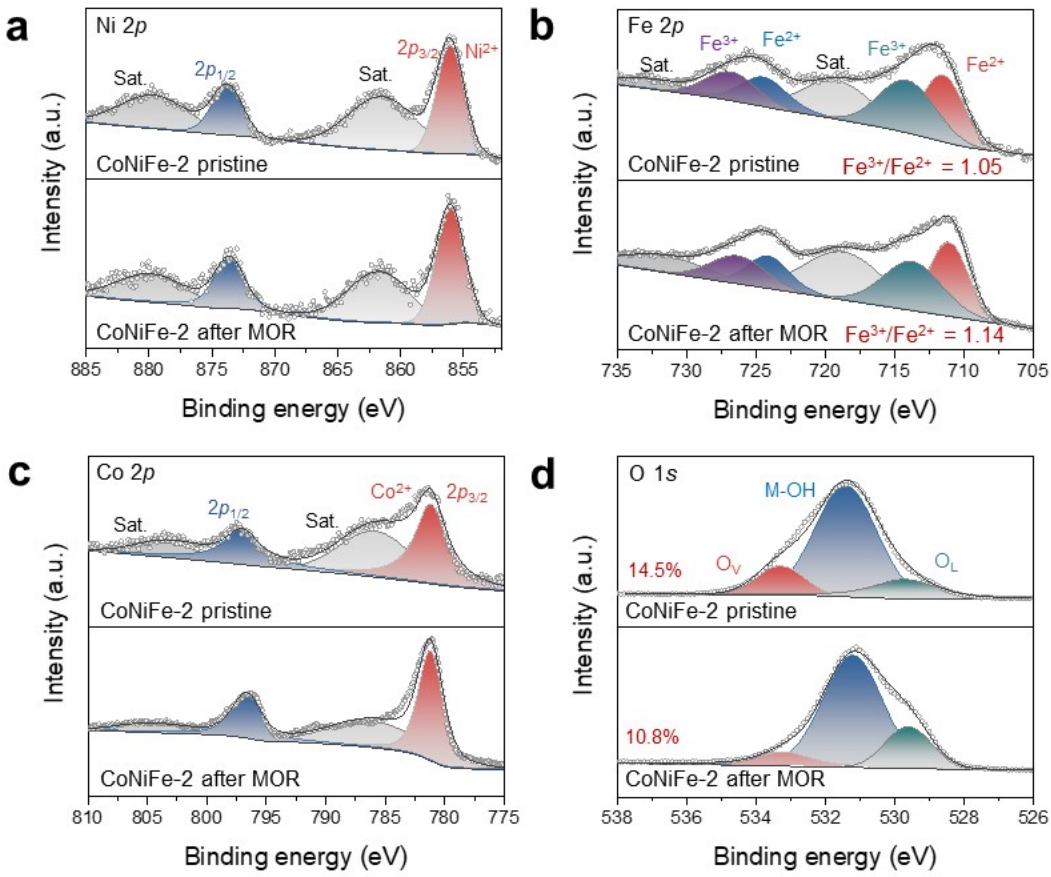

Figure S21. Comparison of (a) Ni 2*p*, (b) Fe 2*p*, (c) Co 2*p*, and (d) O 1*s* XPS spectra of CoNiFe-2 catalyst before and after MOR stability test.

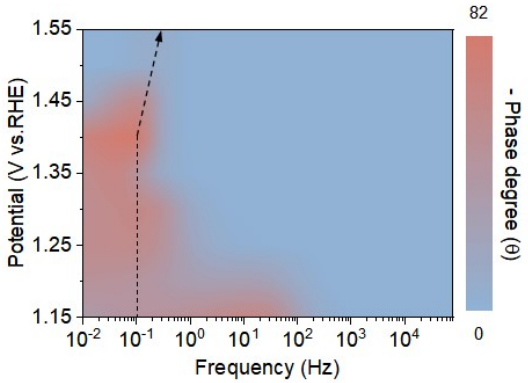

Figure S22. Bode plots of CoNiFe-2 for OER at different potentials.

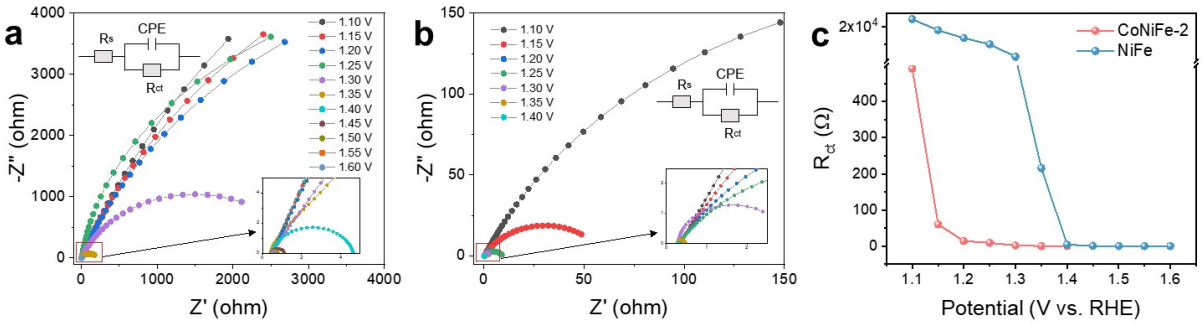

Figure S23. Fitted EIS curves at various potentials in 1 M KOH + 1 M MeOH for (a) NiFe and (b) CoNiFe-2. (c) R_{ct} of NiFe and CoNiFe-2 at different potentials.

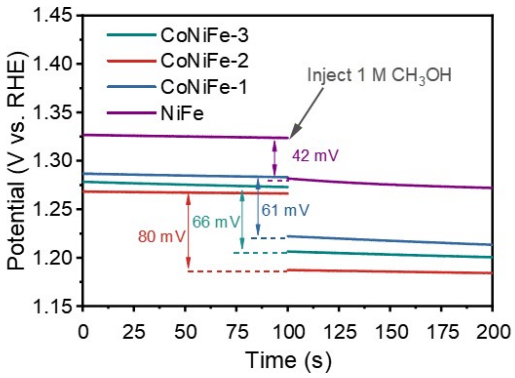

Figure S24. OCP of NiFe and CoNiFe catalysts in 1 M KOH before and after injection of MeOH.

Table S1. ICP-OES results of NiFe, CoNiFe-1, CoNiFe-2 and CoNiFe-3.

Catalysts	Co (wt%)	Ni (wt%)	Fe (wt%)
NiFe	-	12.07	38.04
CoNiFe-1	12.24	8.55	27.82
CoNiFe-2	14.94	7.39	23.89
CoNiFe-3	19.97	5.81	21.60

Table S2. Structural parameters extracted from EXAFS fitting of the Fe K-edge for CoNiFe-2.

Path	CN[a]	R (Å)[b]	σ^2 (Å^2)[c]	ΔE_0 (eV)[d]	R factor
Fe–O	5.85	1.98	0.0078	3.23	0.0081
Fe–O–Ni/Fe/Co	5.52	2.90	0.0069	3.80	

[a]CN, coordination number; [b]R, the distance between absorber and backscatter atoms; [c]σ^2, the Debye Waller factor value; [d]ΔE_0, inner potential correction to account for the difference in the inner potential between the sample and the reference compound; R factor indicates the goodness of the fit.

Table S3. Electrochemical properties of CoNiFe, NiFe and NF.

Catalysts	C_{dl} (mF cm^{-2})	ECSAs (cm^2)	R_s (Ω)	R_{ct} (Ω)
CoNiFe-3	0.68	17.00	0.30	0.96
CoNiFe-2	**0.88**	**22.00**	**0.28**	**0.84**
CoNiFe-1	0.77	19.25	0.25	1.44
NiFe	0.59	14.75	0.23	1.93
NF	0.50	12.5	0.24	2.63

Table S4. The comparison between CoNiFe-2 and other reported non-precious metal-based MOR catalysts.

Sample	Electrolyte	Performance	Reference
CoNiFe-2	**1.0 M KOH+ 1.0 M MeOH**	**1000 mA cm^{-2}/1.37 V *vs*. RHE**	**This work**
$MoO_3/Ni(OH)_2$	1.0 M KOH+ 1.0 M MeOH	1000 mA cm^{-2}/1.40 V *vs*. RHE	*J. Am. Chem. Soc.* 2023, 145, 49, 26858–26862.
CeF_3@Ni_3N/CC	1.0 M KOH+ 1.0 M MeOH	800 mA cm^{-2}/1.45 V *vs*. RHE	*Angew. Chem. Int. Ed*. 2025, 64, e202416763.
NiCo-LDH-E-30/NF	1.0 M KOH+ 1.0 M MeOH	600 mA cm^{-2}/1.42 V *vs*. RHE	*J. Energy Chem*. 2023, 85, 267–275.
Fe-NF-500	1.0 M KOH+ 1.0 M MeOH	650 mA cm^{-2}/1.50 V *vs*. RHE	*Energy Environ. Sci*., 2023, 16, 1100.
Cu_2O-Cu@Ni_2P/NF	1.0 M KOH+ 1.0 M MeOH	600 mA cm^{-2}/1.50 V *vs*. RHE	*Chem. Eng. J*. 2023, 454, 140292.
20% Ni-N-C	1.0 M KOH+ 1.0 M MeOH	600 mA cm^{-2}/1.53 V *vs*. RHE	*Chem. Eng. J*. 2022, 449, 137888.
NiP_x-R	1.0 M KOH+ 1.0 M MeOH	400 mA cm^{-2}/1.40 V *vs*. RHE	*Nat. Commun*. 2022: 13, 2916.
Ni-MOFs@350	1.0 M KOH+ 1.0 M MeOH	400 mA cm^{-2}/1.42 V *vs*. RHE	*ACS Catal*. 2023, 13, 3, 2039–2046.
V-HELH	1.0 M KOH+ 1.0 M MeOH	330 mA cm^{-2}/1.41 V *vs*. RHE	*Small*. 2025, 21, 2411550.
NiFe-LDH/NiFe-HAB/CF	1.0 M KOH+ 1.0 M MeOH	210 mA cm^{-2}/1.50 V *vs*. RHE	*Small*. 2023, 19, 2208027.
F_{10}-Ni_3N	1.0 M KOH+ 1.0 M MeOH	300 mA cm^{-2}/1.57 V *vs*. RHE	*Adv. Mater*. 2025, 37, 33, 2507573.
Co_3O_{4-x}/NF-P	1.0 M KOH+ 1.0 M MeOH	180 mA cm^{-2}/1.39 V *vs*. RHE	*Chem. Eng. J*. 2023, 478, 147288.
$Ni_{0.33}Co_{0.67}(OH)_2$/NF	1.0 M KOH+ 0.5 M MeOH	10 mA cm^{-2}/1.33 V *vs*. RHE	*ChemSusChem*. 2020, 13, 5, 914-921.
NiFe LDH@SnO_2/NF	1.0 M KOH+ 0.5 M MeOH	10 mA cm^{-2}/1.39 V *vs*. RHE	*J. Mater. Sci. Technol*. 2022, 124, 102–108.
Ni-Mo_2C@C	1.0 M KOH+ 1.0 M MeOH	50 mA cm^{-2}/1.43 V *vs*. RHE	*Angew. Chem. Int. Ed*. 2025, 64, e202506215.
Ni-MoN/NF-6	1.0 M KOH+ 0.5 M MeOH	100 mA cm^{-2}/1.48 V *vs*. RHE	*Small*. 2024, 20, 2303300.
Ni-$Bi(OH)_3$/NF	1.0 M KOH+ 1.0 M MeOH	125 mA cm^{-2}/1.54 V *vs*. RHE	*Small*. 2024, 20, 2307741.
NiCo PBA-100	1.0 M KOH+ 1.0 M MeOH	125 mA cm^{-2}/1.56 V *vs*. RHE	*Small*. 2024, 20, 2311452.
Cu/Co NCs	1.0 M KOH+ 1.0 M MeOH	100 mA cm^{-2}/1.58 V *vs*. RHE	*Adv. Sci*. 2025, 12, e05581.

III. References

1. L. Liu, Y. Chen, Q. Zhang, Z. Liu, K. Yue, Y. Cheng, D. Li, Z. Zhu, J. Li and Y. Wang, *Applied Catalysis B: Environment and Energy*, 2024, **354**, 124140.
2. Y. Hao, D. Yu, S. Zhu, C.-H. Kuo, Y.-M. Chang, L. Wang, H.-Y. Chen, M. Shao and S. Peng, *Energy & Environmental Science*, 2023, **16**, 1100-1110.
3. H. Tian, X. Wang, W. Luo, R. Ma, X. Yu, S. Li, F. Kong, X. Cui and J. Shi, *Chemical Science*, 2024, **15**, 11013-11020.